THE JOURNAL OF PHYSICAL CHEMISTRY B

Article

Cite This: J. Phys. Chem. B 2019, 123, 4888−4900

pubs.acs.org/JPCB

Mechanics of the Microtubule Seam Interface Probed by Molecular Simulations and in Vitro Severing Experiments

Lukasz Szatkowski,[†] Dale R. Merz, Jr.,[†] Nan Jiang,[†] Ifunanya Ejikeme,[†] Liudmila Belonogov,[‡] Jennifer L. Ross,[‡] and Ruxandra I. Dima*[,†]

[†]Department of Chemistry, University of Cincinnati, Cincinnati, Ohio 45221, United States

[‡]Department of Physics, University of Massachusetts, Amherst, Massachusetts 01003, United States

Supporting Information

ABSTRACT: Microtubules (MTs) are structural components essential for cell morphology and organization. It has recently been shown that defects in the filament's lattice structure can be healed to create stronger filaments in a local area and ultimately cause global changes in MT organization and cell mobility. The ability to break, causing a defect, and heal appears to be a physiologically relevant and important feature of the MT structure. Defects can be created by MT severing enzymes and are target sites for complete severing or for healing by newly incorporated dimers. One particular lattice defect, the MT lattice "seam" interface, is a location often speculated to be a weak site, a site of disassembly, or a target site for MT binding proteins. Despite seams existing in many MT structures, very little is known about the seam's role in MT function and dynamics. In this study, we probed the mechanical stability of the seam interface by applying coarse-grained indenting molecular dynamics. We found that the seam interface is as structurally robust as the typical lattice structure of MTs. Our results suggest that, unlike prior results that claim the seam is a weak site, it is just as strong as any other location on the MT, corroborating recent mechanical measurements.

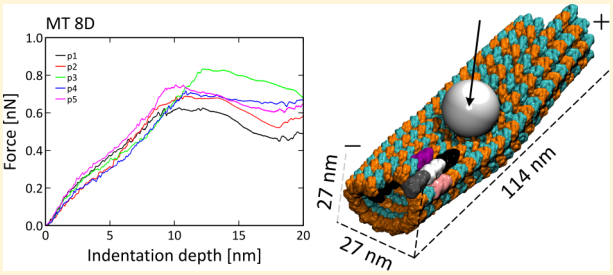

INTRODUCTION

Microtubules (MTs) are made of α−β-tubulin heterodimers joined longitudinally into protofilaments (PFs), which associate laterally to form a hollow cylindrical structure.[1] Although most MTs in cells contain 13 PFs, MTs with other PF numbers (ranging from 8 to 20) have been observed *in vitro* and *in vivo*.[2,3] The MT filament is polar in structure, with the plus end exposing the β-tubulin subunits and the minus end exposing α-tubulin (see Figure 1C, where α-tubulin is in orange and β-tubulin is in cyan). Tubulin dimers are GTPases where one GTP binds per monomer.[4] Upon entropically driven polymerization into MTs, GTP bound to the β-tubulin subunit hydrolyzes to release the energy needed to disassemble the MT.[5] The stochastic switching between polymerization and depolymerization is called dynamic instability, and it is used to control the location of MTs within the cytoskeletal networks of cells in space and time.

The lattice structure of most MTs is primarily a "B-lattice", corresponding to α−α and β−β lateral contacts between monomers. However, upon assembly into a closed filament, some PF numbers result in a different lattice at the closure position. This altered lattice location is called a "seam" corresponding to a helical shift of 3 monomers between the first and the last PFs resulting in lateral contacts. The lattice type at the seam is an A-lattice where there are lateral contacts between α- and β-tubulin monomers[2] (represented by the magenta region in Figure 1D).

The MT seam has been suggested as a possible dislocation defect in the lattice. It has also been proposed that the seam is a trigger location for the depolymerization because it is speculated to be a weak point of the MT lattice,[6] but this view remains controversial.[7] Support for the role of the seam in MT dynamic instability came from recent high-resolution cryo-electron microscopy (cryo-EM) structures for MTs in different nucleotide states and with different binding partners.[8] The view arising from these studies is that the fundamental change in the MT lattice during the GTPase cycle is the compaction of tubulin dimers at the longitudinal interface accompanied by a gradual destabilization of lateral contacts between PFs, particularly at the seam.[8,9] These results suggest that the seam will lose lateral contacts after GTP hydrolysis, creating a crack at that location. Such a crack would generate a large lattice defect at the seam. Another possible role for the seam serving to destabilize MTs could be due to its relation to destabilizing enzymes. Prior studies have suggested that MT severing enzymes specifically target lattice defects,[10−13] although it is still unknown if the seam is a target for these enzymes.

Despite evidence that the seam should be a defect or mechanically weak location, several recent studies have

Received: April 1, 2019
Revised: May 15, 2019
Published: May 22, 2019

DOI: 10.1021/acs.jpcb.9b03059
J. Phys. Chem. B 2019, 123, 4888−4900

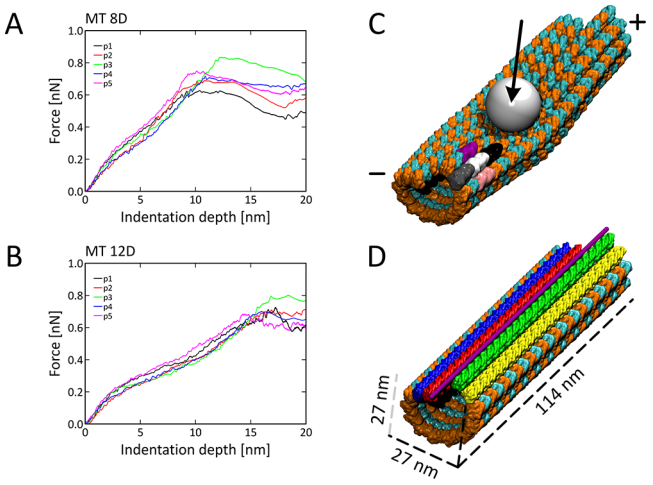

Figure 1. Simulation setup and force data. (A) Average force versus indentation depth curves for the 8D MTs at each indentation position (runs without the plate). (B) Similar to part A, but for the 12D MT runs. (C) Indentation setup for pushing on the seam (cantilever sphere in gray, the direction of the applied force as the black arrow, oriented orthogonally down on the MT outer-surface). The MT subunits are colored in orange (α-tubulin) and cyan (β-tubulin). The minus and plus end of the filament are indicated. The N, S, E, W neighboring dimers for a particular dimer (white) are indicated in black, gray, pink, and magenta, respectively. These cardinal directions follow the orientation of polymerization in MTs from the minus to the plus end. (D) The dimensions of the 12D MT filament and the 4 PFs involved directly in indentation. For position p1, push between P12/P13 (red/blue PFs); position p2, push on P13 (red PF); position p3, push between P1/P13 (seam) (between green/red PFs); position p4, push on P1 (green PF); and position p5, push between P1/P2 (green/yellow PFs). The seam is in magenta. Snapshots here and in all other figures were produced using the VMD package.[20] Note that capital P# stands for PF number, while small p# for position of indentation.

provided evidence to the contrary. One recent study directly measuring the persistence length of freely fluctuating MT filaments demonstrated that MTs with high levels of seam defects had the same bending modulus as regular MTs.[14] These MTs with mixed A- and B-lattice structures are created by polymerizing tubulin in the presence of high concentrations of NaCl. Such "high-salt" MTs have numerous seams (50%) caused by PF shifts.[15] These prior results suggest that the seam is not weaker than the typical B-lattice structure. Further, using cryo-EM, recent studies have demonstrated that the density of interprotofilament interactions in the seam region is similar to that between PFs in the B-lattice part of the filament, suggesting that the seam's A-lattice should have the same mechanical stability as the rest of the B-lattice of the MTs.[2]

Ultimately, studies probing directly the mechanics and the thermodynamics of the seam at the microscopic level are needed to understand the seam and its possible role in the severing of an MT filament. With this goal in mind, we investigated the role of the seam in the mechanical behavior of the filament, as relevant for example during removing dimers (such as in severing). We performed simulations of the seam under compression forces using the computational framework from our previous studies of the indentation of MT lattices[13,16] mimicking atomic force microscopy (AFM) indentation experiments.[17] Our results show that the critical forces required to break the lattice at or in the vicinity of the seam are indistinguishable from the forces required to break defect-free lattices at regular B-lattice interfaces, exceeding the force that a AAA+ ATPase could exert.[18] Using a combination of indentation and retraction simulations, in conjunction with a fluctuation−dissipation theorem,[19] we determined that the strength of contacts at the seam is comparable with that for other lateral contacts in a 13 PF MT lattice.[16] These results support the idea that the seam is not a lattice defect or a mechanically weak location.

Furthermore, to probe the role of the seam during the severing of MTs by katanin, a MT severing protein, we directly measured katanin activity on high-salt MTs. We found that the bending behavior of MTs with mixed A- and B-lattices (high-salt MTs) or of control MT lattices with only one A-lattice in the filament in the severing assays is closely reproduced by our simulated bending of long filaments, which lends credence to the ability of our simulation approach to shed light on the process of MT severing. Moreover, as the two distributions of bending angles for high-salt and, respectively, control MTs are identical statistically, we posit that the seam is not a likely target for severing proteins such as the katanin used in the severing assays.

METHODS

Theory and Computational Details. *Total Potential Energy for the SOP Model.* We used the self-organized polymer (SOP) model and Brownian dynamics for all our simulation runs.[21] For acceleration, we employed the graphics processing units (GPUs) based version of the SOP software, called gSOP (versions 1.07 and 2.0).[22] The SOP model uses a finite extensible nonlinear elastic (V_{FENE}) potential for the covalent bonds, a Lennard-Jones potential for the noncovalent, nonbonded interactions (V_{NB}^{ATT}), and the repulsive part of the Lennard-Jones potential for all the non-native, nonbonded interactions (V_{NB}^{REP}). The total potential energy (V_T) of a protein in the SOP model is

$$V_T = V_{FENE} + V_{NB}^{ATT} + V_{NB}^{REP} \tag{1}$$

$$V_{FENE} = \sum_{i=1}^{N-1} \frac{k}{2} {R_0}^2 \log\left(1 - \frac{(r_{i,i+1} - r_{i,i+1}^0)^2}{{R_0}^2}\right) \tag{2}$$

$$V_{NB}^{ATT} = \sum_{i=1}^{N-3} \sum_{j=i+3}^{N} \epsilon_h \left[\left(\frac{r_{ij}^0}{r_{ij}}\right)^{12} - 2\left(\frac{r_{ij}^0}{r_{ij}}\right)^6\right] \Delta_{ij} \tag{3}$$

$$V_{NB}^{REP} = \sum_{i=1}^{N-2} \epsilon_l \left(\frac{\sigma_{i,i+2}}{r_{i,i+2}}\right)^6 + \sum_{i=1}^{N-3} \sum_{j=i+3}^{N} \epsilon_l \left(\frac{\sigma}{r_{ij}}\right)^6 \times (1 - \Delta_{ij}) \tag{4}$$

The parameter ϵ_h represents the strength of the native contacts in the lattice. Moreover, this is the only parameter from the potential energy function that changes based on the type of contact and the type of topology investigated. The remaining parameters in the potential were k = 20.0 kcal/mol·Å^2, R_0 = 2.0 Å, and r_i = 3.8 Å, for i = 1, 2, ..., N, where N is the total number of residues. $r_{i,j}$ represents the distance between two residues, i and j, while $r_{i,j}^0$ is its value in the native structure. For the nonbonded part of the potential energy, two residues i and j where ($|i - j| > 2$) are considered to be in contact if their Cα positions are within a cutoff of R_c = 8.0 Å; inside the cutoff distance, Δ_{ij} = 1 and outside it is zero. That is, we generated the contact topologies for any input structure using an 8 Å

DOI: 10.1021/acs.jpcb.9b03059
J. Phys. Chem. B 2019, 123, 4888−4900

cutoff criterion with each amino acid represented by its Cα position. We also used σ = 3.8 Å, and ϵ_l = 1 kcal/mol.

Parameterization of the MT Models. We constructed MTs comprised of 13 PFs with varied numbers of dimers per PF (8, 12, and 16) to account for any finite-size effects, as described in detail in the Section I.1 in the Supporting Information. Following our previous work,[13,16] initially we built a single ring of 13 dimers based on the atomistic structures for sets of PFs.[23] These rings were duplicated and placed longitudinally, oriented from the α to the β end until the appropriate dimer length was reached (Figure S1A).

As described above, the contact strength in the Lennard-Jones potential is set by the well-depth, ϵ_h. For our regular (Reg) model, we set ϵ_h to 1.9 kcal/mol for the strength of the intradimer contacts, 1.0 kcal/mol for the longitudinal contacts, and 0.9 kcal/mol for the lateral contacts, following the parametrization from our previous work,[16] which is also described in detail in ref 13. We investigated other topologies representing MT states characterized by different strengths of the various lateral and longitudinal interfaces, following our previous work.[13] The types of MT structures are (1) a lattice, otherwise regular, which corresponds to strengthened interactions between PFs P5 and P6 (PF5-PF6), (2) an MT lattice corresponding to a lateral homogeneous model (LHM) where all lateral interfaces are changed to the same overall energy value, and (3) an MT lattice corresponding to an all homogeneous model (AHM) where, on top of the LHM constraints, we set also the longitudinal interactions to the average energy per longitudinal interface.[13] In all these models, we kept the seam interactions the same (ϵ_h = 0.9 kcal/mol), corresponding to a lower level of mechanical strength, which is about half of the average strength of the other PF−PF lateral interfaces. This is in agreement with the results of atomistic simulations, which found that the lattice in the GTP state is characterized by a homogeneous energetic distribution of lateral and longitudinal interfaces.[24] Among these models, we used primarily the AHM and Reg MTs in our simulations because they most closely represent the two main MT nucleotide binding states: GTP-MT (AHM) and GDP-MT (Reg).[13]

Simulations Setup and Analysis. As shown in Figure 1, we used a cantilever, implemented as a rigid sphere with radius R_{tip} = 10 nm, similar to the diameter of the katanin and spastin hexamers,[25] for the indentation simulations. The cantilever induced fracturing of the MT at a speed of 2.0 μm/s, similar to the experimental indentation speed in AFM experiments.[17] We ran simulations where the MTs rested on a plate, recalling the AFM experimental setup, as well as simulations where the MTs were simply held fixed at the ends, suspended in free space, to mimic the typical conditions in the cytosol. The interactions between all the protein positions with both the plate and the cantilever are modeled using the repulsive part of the standard Lennard-Jones potential, $V_{LJ} = \epsilon_{LJ}(\sigma_{LR}/(r_i - R_{tip}))^6$, where ϵ_{LJ} = 4.18 kJ/mol, σ_{LR} = 1.0 Å is the distance between the center of the sphere representing the tip and an amino acid, r_i is position of the ith particle, and R_{tip} = 10 nm is the radius of the tip. The cantilever spring constant was k_s = 50 pN/nm, in accord with the value from AFM experiments. We oriented the force toward the surface, perpendicular to the long axis of the filament (see Figure 1C). In the majority of our indentation and retraction simulations, except where specifically noted, the MT cylinder was placed with the seam side up.

Similar to our previous studies,[13,16] we selected multiple positions for indentation to probe the mechanical response of the lattice in the vicinity of the seam. Namely, we investigated five indentation positions, longitudinally centered: position p1, west of the seam, pushing the lattice between PFs P12 and P13; position p2, west of the seam, pushing the lattice on PF P13; position p3, at the seam, pushing the lattice between PFs P13 and P1; position p4, east of the seam, pushing the lattice on PF P1; position p5, east of the seam, pushing the lattice between PFs P1 and P2 (the numbering of the PFs in the MT lattice is in Figure S1A and the indentation positions and the cardinal directions are illustrated in Figure 1D).

We ran Brownian dynamics simulations at 300 K, with an integration time step of 40 ps, corresponding to a unitless friction coefficient for a residue in water ζ = 50.0. The time step resulted from h = 0.16 τ_H given that $\tau_h = \frac{\zeta \epsilon_h}{k_B T}\tau_L$ and τ_L = 2.0 ps, as in our previous work.[13] A frame in any of our plots corresponds to 40 μs. We ran multiple trajectories while varying the point of contact with the MT lattice, holding both ends of an MT filament fixed or only one end fixed, and with and without a plate. The number of trajectories for each indentation setup is listed in Tables S1 and S2 in the Supporting Information for the simulations with both ends fixed and, respectively, with only the minus end fixed. Following our previous studies[13,16] and related experiments,[26] for selected indentation runs, we carried out retraction simulations, i.e., where we decrease linearly the force to zero. To determine the role played by the plate in the recovery of the structure of the filament, we ran retractions with and without the plane (see Table S3). Data analysis of the simulation runs, including the analysis of the force−indentation and retraction curves, the time evolution of contacts for dimers, and details about procedures to measure the bending angles for the MT lattice are in sections I.2−3 and Figure S2 and Figure S3 from the Supporting Information.

EXPERIMENTAL SECTION

Protein Reagents. Unless otherwise stated, chemicals were purchased from Sigma-Aldrich (St. Louis, MO). Tubulin proteins that were unlabeled or rhodamine-labeled were purchased from Cytoskeleton (Denver, CO) as lyophilized powder. We used an human katanin p60 construct with a maltose binding protein (MBP) and green fluorescent protein (GFP) optimized for bacterial expression (GeneWiz, Cambridge, MA), as previously described.[27] An IPTG inducible expression system was used to express and the MBP tag was used for affinity purification. The plasmid was transformed into BL21 competent *Escherichia coli* (New England BioLabs, Ipswich, MA). A starter culture was grown overnight and added to a 500 mL culture the next day that was grown at 37 °C until it reached an OD of 0.8 before being induced with 1 mM IPTG. The culture continued to grow at 16 °C for 16 h. Cells were lysed in resuspension buffer (20 mM HEPES-HCl pH 7.7, 250 mM NaCl, 0.5 mM β-mercaptoethanol, 10% glycerol, 0.25 mM ATP) via sonication. The lysate was incubated with amylose resin (New England BioLabs, Ipswich, MA) for 1−2 h. The lysate/resin mixture was added to a column and allowed to enter the column completely. Once excess lysate had passed through the column, the column was washed twice with 20 mL of resuspension buffer. Then the protein was eluted in elution buffer (20 mM HEPES-HCl pH 7.7, 250 mM NaCl, 0.5 mM β-mercaptoethanol, 10% glycerol,

DOI: 10.1021/acs.jpcb.9b03059
J. Phys. Chem. B 2019, 123, 4888−4900

0.25 mM ATP, 10 mM maltose) at 4 °C. The concentration was determined using a Bradford assay.

Microtubule Polymerization. To polymerize control MTs, unlabeled and labeled tubulin was resuspended in PEM-100 (100 mM K-PIPES, pH 6.8, 2 mM $MgSO_4$ 2 mM EGTA) to a concentration of 5 mg/mL. Both were incubated on ice for 10 min. The labeled and unlabeled tubulin were combined (10% labeled) and centrifuged at 366 000 × *g*, 4 °C for 10 min to remove aggregates. To polymerize the MTs, 1 mM GTP was added to the tubulin (supernatant) and was incubated at 37 °C for 20 min. To stabilize the MTs, 50 μM paclitaxel (Taxol) was added and MTs were incubated for 20 min at 37 °C. The MTs were centrifuged at 16 200 × *g*, 27 °C for 10 min. The pellet was resuspended in PEM-100 and 50 μM Taxol. To polymerize MTs with seam defects, tubulin was hydrated, combined, and centrifuged, as for control MTs. The supernatant was supplemented with 1 mM GTP and 580 mM NaCl (Acros Organics, New Jersey). As with control MTs, seam defect MTs were polymerized by incubating at 37 °C for 20 min, stabilized by the addition of 50 μM paclitaxel, and equilibrated by incubating at 37 °C for 20 min. MTs were centrifuged at 25 °C for 10 min to remove unpolymerized tubulin. MTs were resuspended in the original volumes of PEM-100 with 50 μM Taxol. Cartoon representations of control and high-salt MTs are in Figure S1B.

In Vitro Severing Assays. We made a 10 μL flow chamber with double stick tape (3M), a slide, and a silanized coverslip (No. 1.5 Fisherbrand, Thermo Scientific). The silanized coverslips were made by cleaning with acid and coating with 2% dimethyldichlorosilane (GE Healthcare, Wauwatosa, WI) to create a hydrophobic surface.[28] Chambers were coated with 2% (w/v) MAB1864 tubulin antibody (YL1/2, Merck-Millipore, Billerica, MA) in Katanin Activity Buffer (20 mM HEPES-HCl pH 7.7, 10% glycerol, 2 mM MgCl2). Next, we added 5% (w/v) Pluronic F-127, a block copolymer in Katanin Activity Buffer to block the surface not bound with antibodies. Next, fluorescent, Taxol-stabilized MTs (control or seam defect MTs) were added and incubated in the chamber for 5 min. To remove excess MTs, Severing Buffer (20 mM HEPES-HCl pH 7.7, 10% glycerol, 2 mM MgCl2, 2 mM ATP, 0.025 mg/mL BSA, 0.05% F-127, 10 mM DTT, 15 mg/mL glucose, 0.15 mg/mL catalase, 0.05 mg/mL glucose oxidase) was flowed into the chamber. The MTs were imaged for 3 min to ensure MTs were present and bound to the surface. Next, Severing Buffer with GFP-labeled human katanin p60 was flowed into the chamber during imaging. The protocols and buffers have been described in several prior studies by other groups and ourselves.[11,27,29−31]

Imaging was performed using epi-fluorescence and total internal reflection fluorescence (TIRF) a Nikon Ti-E microscope with a home-built laser illumination system.[32] The objective was a 60×x (1.49 NA) oil immersion with an additional 2.5× or 4× magnification prior to the camera (Andor, IXON, EM-CCD), which caused a pixel size of 108 or 67.5 nm per pixel, respectively. MTs were imaged using epi-fluorescence in the rhodamine channel (ex: 540, em: 605). GFP katanin-p60 was imaged using TIRF illuminated with a 488 nm laser (Melles Griot), and the high-signal-to-noise TIRF images were used for the kinking analysis. GFP images were collected at 16.7 frames/s without delay (60 ms per frame) using an EM-CCD camera with EM-gain set at 300. We measured the kinking angles for data taken at two different katanin concentrations, 50 nM and 100 nM. The progress of severing for these data sets was previously reported and progressed normally.[13,27]

Kinking Angle Analysis. We used the analysis to measure kinking angles described in previous publications.[10,13] We followed the kinking and breaking of individual MTs in time using TIRF microscopy (Figure 2). Movies were imported as nd2 files from Nikon Elements into Fiji/ImageJ. The movie was run forward to find the breaking position and frame of breaking. The angle tool was employed to measure the angle at the ultimate breaking point over time. For 10 frames prior to kinking, the angle was recorded for all frames until the MT was severed completely at the kinking site (Figure 2).

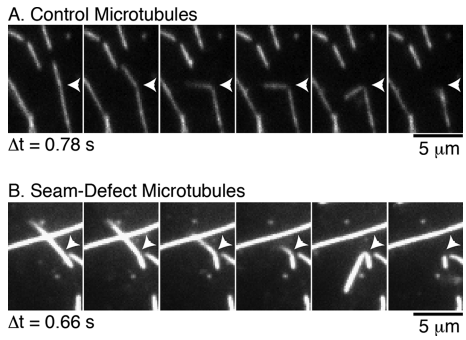

Figure 2. Timeseries of (A) control MTs, and (B) high-salt MTs as they were being severed by katanin causing the lattice to be cut, to kink and fluctuate, and eventually to lose contact. Arrowheads denote the kinking location where the angle was measured. The time between frames was 0.78 s for control and 0.66 s for high-salt MTs. Scale bars indicate 5 μm in length.

The measured kinking angles were reported as 180° for a straight, unkinked filament to 0° if the filament was completely folded doubled over. We converted the angles to correspond to the coordinates needed to compare to data such that a straight MT was kinked 0° and a doubled over filament was 180°. Kinking angle data was analyzed by creating cumulative distribution functions (CDFs). We did not include the data from early, unkinked times, before severing began, similar to prior works.[10,13]

RESULTS AND DISCUSSION

Force Distribution for Indentation near the Seam Recalls the Behavior of the B-Lattice Regions. We focused on quantifying how the mechanical response of a MT filament varies between the seam (the A-lattice part) and the regular B-lattice regions by extracting from each indentation trajectory two force values: the initial breaking force and the critical breaking force, as depicted for the indentation position p1 in Figure S4. These would be relevant during severing: the initial breaking force quantifies how difficult it is to start the cutting of a MT lattice, and the critical force corresponds to the maximum work required to finish the severing process. We found that the cut through lattice interfaces can be highly reversible between the initial and critical stages (detailed in section II.2 of the Supporting Information). Our simulations show that both the force needed to start breaking the MT structure and the critical force are as high in the vicinity of the seam as for the regular B-lattice regions (Table 1).

The seam (A-lattice region) indentation simulations show that the initial breaking force on or near the seam is between 0.31 and 0.47 nN (see Table 1 for averages over all setups,

DOI: 10.1021/acs.jpcb.9b03059
J. Phys. Chem. B 2019, 123, 4888−4900

Table 1. Average Forces from Different Indentation Setups with Both Ends of the Filament Fixed[a]

simulation setup	first breaking force/nN	critical force/nN
MT 8D with plate	0.46 ± 0.03	0.73 ± 0.07
MT 8D without plate	0.46 ± 0.02	0.73 ± 0.08
MT 12D with plate	0.37 ± 0.05	0.72 ± 0.11
MT 12D without plate	0.36 ± 0.03	0.71 ± 0.08
MT 16D without plate	0.31 ± 0.00	0.75 ± 0.03
MT 8D seamdown intact[b]	0.50 ± 0.08	0.75 ± 0.11
MT 8D seamdown defects[b]	0.29 ± 0.10	0.53 ± 0.09

[a]The distributions are in Figure 3. The full data for each type of setup is in Table S1 and select runs are depicted in Figure S5. Table S2 reports the corresponding data for the simulations with the plus end free, with select runs depicted in Figure S6. [b]Data from ref 13.

Tables S1 and S2 in the Supporting Information for separate averages for each setup, and select runs depicted in Figure S5 and Figure S6). Moreover, the values for the 8D long filament are close to those for the intact MTs of the same length (~ 0.50 nN) from the B-lattice regions.[13] We also found that the first breaking force decreases with the increase in the length of the filament, leading to minimal overlap between the respective distributions for the 8D and 12D systems (Figure 3A and left panels in Figure S7). Once the lattice undergoes the first break, one can no longer distinguish energetically between the 8D and 12D lattices as the distributions of the critical breaking forces are the same (Figure 3B and right panels in Figure S7). This behavior is a manifestation of the fact that the MT lattice before and after the first break represents in fact different polymers.[16] Indentation directly on the seam led to the highest critical breaking forces (~ 0.84 nN) but average first breaking forces (0.46 nN for 8D and 0.35 nN for 12D). In contrast, pushing on either of the two PFs adjoining the seam (P1 or P13) led to the lowest first breaking forces (0.45 nN for 8D and 0.33 nN for 12D) and average critical forces (0.71 nN). Thus, in accord with our previous work,[13] the indentation on a PF requires the least amount of force to start the cutting action. Finally, we found that the plate has little impact on the brittleness of the MT lattice, as seen in the similarity of the respective force plots (Figure S5).

Importantly, our results correlate well with the results of AFM indentation experiments. For example, we found that the initial breaking occurs at indentation depths between 4 and 10 nm (see Figure 1 and Figure S5) when AFM experiments detected a force signal of 0.3 nN at an indentation depth of 5 nm.[26] Moreover, the distribution of breaking forces from experiments (Figure 1 in ref 17) of 0.25−0.60 nN matches well the distribution of forces from our simulations (Table 1).

Breaking Pathways for Indentation near the Seam. The initial response of the MT lattice under indentation by the AFM-like tip (sphere) is flattening and buckling, an example of elastic deformation, which recalls the literature result that local buckling (kinking) can occur in a thin-walled tube due to cross-sectional ovalization.[33] However, because a MT filament is a collection of PFs arranged in parallel around a cylinder, rather than a continuous tube or shell, we found deviations from literature findings: the buckling (kinking outward) of the PFs on the sides of the lattice is correlated with a tightening of the lateral interface(s) located under and/or near the tip (corresponding to increases by 50% to 100% in the number of contacts seen in Figure 4 and in Figure S8) due to the inward bending of the corresponding PFs (see the second stage from Figure 5). This dynamic local hardening leads to an increase in the first breaking force, rather than the decrease seen for thin continuous shells.[34] The differential (outward versus inward) kinking style of the PFs becomes more pronounced once a few lateral interfaces rupture, as seen in the later stages in Figure 6, due to the loss of correlated bending motions of the PFs.

In our simulations the first break occurs at lateral interfaces between PFs located under or very close to the end of the MT both at the seam and other nearby PF to PF interfaces. This is a manifestation of the transition of the lattice from an elastic to a more plastic or brittle behavior. We also found that the presence of the plate limits the degree of damage to the lattice, irrespective of the length of the MT filament. In what follows, we will provide an overview of the most important findings about the breaking pathways, while the detailed description of the pathway for each type of indentation setup is in section II.1 of the Supporting Information. Snapshots along the various pathways for the MT 12D lattice case are depicted in Figure S9.

Simulations for MTs with Both Ends Fixed. *Indentation on the Seam (Position p3).* For all MT lengths (8D, 12D, and 16D) we found that the initial breaking event corresponds to the loss of lateral interactions at the seam, followed by the breaking of multiple longitudinal interfaces from PFs in the neighborhood of the seam. The simulations without the plate result in the largest number of breaks at the various interfaces. Thus, the plate delays the loss of MT

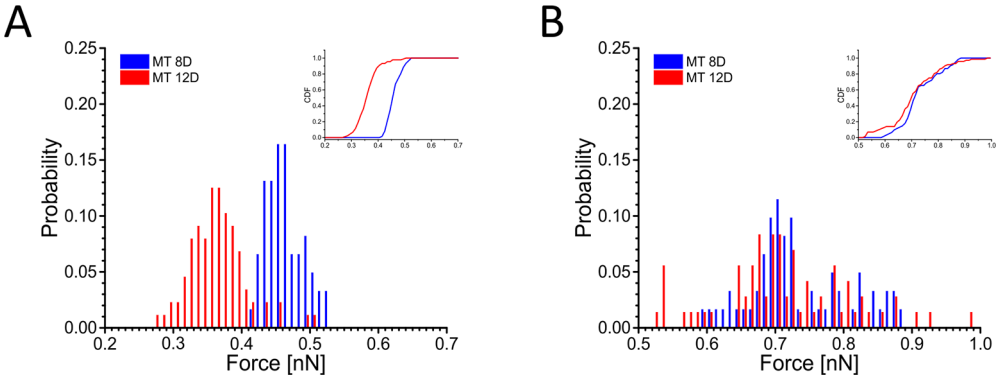

Figure 3. Distribution of first and critical breaking forces for MT 8D (blue) and 12D (red) simulations with both ends fixed. (A) First breaking forces. (B) Critical breaking forces. The insets represent the corresponding CDFs. The respective distributions for each type of indentation position are in Figure S7.

DOI: 10.1021/acs.jpcb.9b03059
J. Phys. Chem. B 2019, 123, 4888−4900

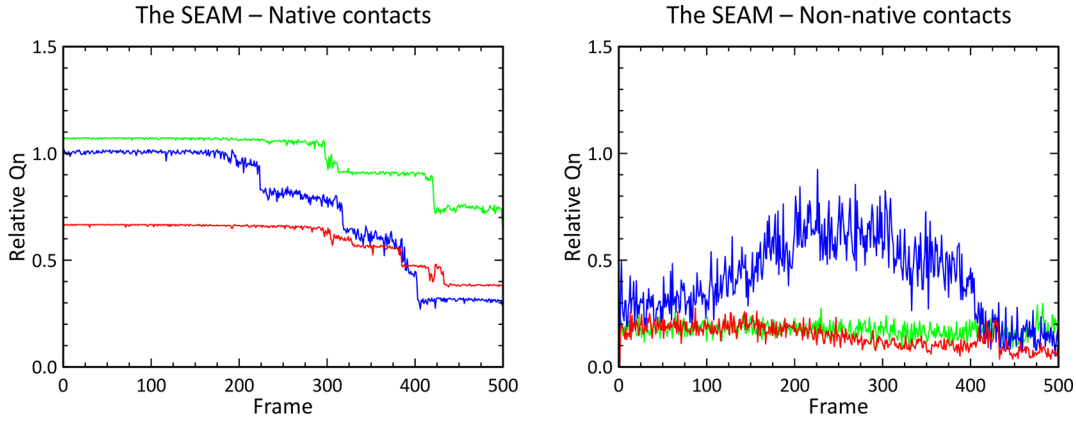

Figure 4. Time evolution of the native and non-native contacts at the seam for the MT 8D with ends fixed indented on the seam (position p3). The *y*-axis reports the relative Q_u, which is the total number of contacts (native or non-native) for an interface at each frame divided by the average value of the native contacts for that type of interface (lateral, longitudinal, or seam) in the starting configuration. Key: left panel, native; right panel, non-native; green, P1 longitudinal contacts; blue, P1/P13 lateral contacts; red, P13 longitudinal contacts.

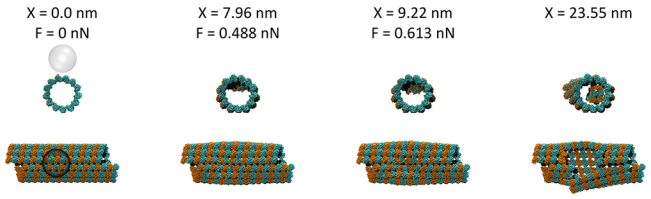

Figure 5. Steps along the pathway for indentation on the seam (position p3) for the MT 8D lattice with both ends fixed. For each stage, we list the indentation depth and the force exerted by the mimic of the cantilever sphere. The last conformation corresponds to the end of the trajectory when the sphere almost touches the lower wall of the filament. Colors for the tubulin dimers follow the scheme from Figure 1. Each stage is represented both along the main axis of the filament view and the top view. For the starting stage, we also depict the indentation sphere, and we circle the indented region.

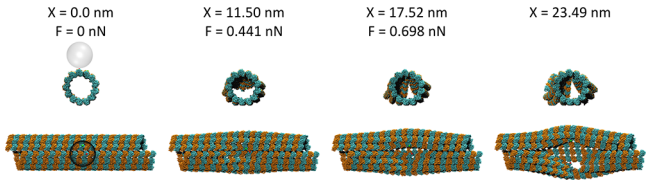

Figure 6. Steps along the buckling pathway for indentation on P1 (position p4) for the MT 12D lattice with both ends fixed. The figure follows the setup from Figure 5.

structure under radial stress applied on the seam. Finally, we found that the total number of lattice breaks for the longer filaments is more modest than for the MT 8D lattice, which is indicative of finite-size effects in the mechanical response of the MT 8D filament. As discussed above, we detected the formation of a substantial number of non-native contacts in the neighborhood of the pushing sphere: the seam gains up to 75% non-native contacts along this pathway in the 8D filament (blue curve in the left panel of Figure 4) and up to 50% non-native contacts in the 12D filament (blue curve in the left panel of Figure S8A). This leads to the local hardening of the filament prior to the first breaking event. All the non-native contacts formed at the seam are still in the A-lattice configuration. Representative states along this pathway are presented for the MT 8D case in Figure 5 and for the 12D case in Figure S9B. Notably, at the end of this trajectory, a substantial gap corresponding to 3 × 3 missing subunits opens in the upper surface of the MT filament and side PFs break longitudinally and protrude outward from the lattice (Figure 5).

Indentation on PFs Neighboring the Seam (Position p2, on P13; and Position p4, on P1). The pathway followed by these simulations is the same irrespective of the length of the MT filament and the presence of the plate. For both indentation positions the first event is the lateral rip at the seam. Further events correspond to multiple longitudinal breaks and lateral cracks in the PFs surrounding the seam. In these trajectories the longitudinal break, which occurs right after the seam rips, is on the pushed PF. This is followed closely by longitudinal breaks in its two nearest neighbor PFs. The evolution of native and non-native contacts at the seam along these pathways in the 12D MTs is depicted in Figure S8D for p2 and Figure S8E for p4, and it follows the pattern discussed above for indentation positions p1−p5. Representative states along this pathway are presented for the MT 12D case in Figure 6.

Indentation on PF P3. Because in all our above simulations we found that the seam breaks early during the run, but only under substantial applied forces due to the local hardening of its contacts, we set out to explore a setup that can take advantage of any weakness of the seam without the potential hardening resulting from its close placement under the indentation sphere. We selected the lattice orientation that places the two weakest lateral interfaces (the seam and P5/P6) equidistantly from the point of indentation, allowing them to experience the external perturbation under identical conditions: pushing on PF P3. We only ran simulations for the MT 8D filament. As above, we found an initial flattening of the MT under the tip, corresponding to the ovalization of the cross-section, which is correlated with a partial loss of contacts at the two weakest lateral interfaces, as seen in the monotonic decrease of their native contacts starting at frame ∼200 in Figure 7. Despite our expectation that interfaces located farther away from the indentation sphere will not undergo contact hardening, we found an accumulation of non-native contacts at the side interfaces (Figure 7) leading to the buckling of the respective PFs. Expected increases in the number of non-native contacts (up to 50% of the original number of native contacts)

DOI: 10.1021/acs.jpcb.9b03059
J. Phys. Chem. B 2019, 123, 4888−4900

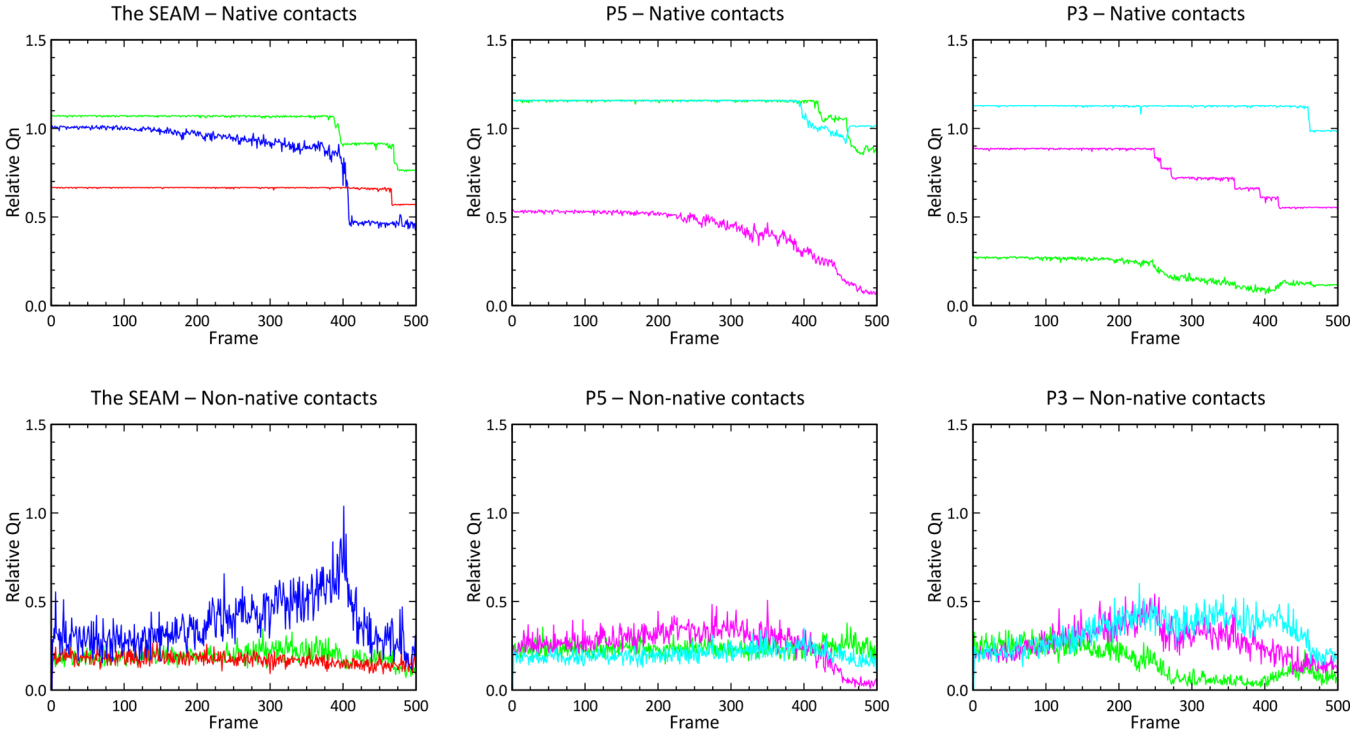

Figure 7. Time evolution of the native and non-native contacts for the MT 8D with ends fixed indented on PF 3 P3. The *y*-axis reports the relative Q_u (same as in Figure 4). Left panel (the seam, position p3): green, P1 longitudinal contacts; blue, P1/P13 lateral contacts; red, P13 longitudinal contacts. Middle panel (P5): green, P5 longitudinal contacts; magenta, P5/P6 lateral contacts; cyan, P4/P5 lateral contacts. Right panel (P3): green, P3 longitudinal contacts; magenta, P3/P4 lateral contacts; cyan, P2/P3 lateral contacts.

occur for the lateral interfaces made by P3 with its neighboring PFs (Figure 7).

We found two pathways for this setup: the minor one follows the typical breaking pathway for pushing on MT 8D with both ends fixed described above, while for the major pathway (75%), there is no time/frame separation between the initial and critical breaking events because both lateral (P2/P3 and/or P3/P4) and longitudinal (P3(R3) or P3(R4); where R indicate the ring number from the minus end) breaks on the pushed PF P3 occur simultaneously, resulting in pushing the indented dimer inside the MT. The average breaking force of ~0.52 nN (Table S1) is slightly higher than the average first breaking force for the 8D MTs, but substantially lower than the critical breaking force for MT 8D from Table 1. The indentation leads to an increase in the number of non-native contacts at the seam (Figure 7) up until it becomes comparable to the original number of native contacts and the seam rips. Thus, placing the seam at the side of the filament leads to the lowering of the critical breaking force. Interestingly, this is the only case when the MT lattice has a brittle response to indentation, suggesting that a filament with weak lateral interfaces at its sides cannot withstand radial compression once a crack appears in the lattice.

Simulations for MTs with the Plus End Free. All trajectories for this type of simulations start with the relaxation of the MT filament, i.e., elongation along the long axis of the cylinder. This behavior recalls the straightening of dimers in the GTP lattice versus their bent, compressed conformations in the GDP lattice.[35] The indentation leads to the ovalization of the MT not only under the tip, similar to the above behavior of the MT with both ends fixed but also at the free plus end, as seen in the later stages from Figure 8. Moreover, here we pushed not only on positions in the neighborhood of the seam

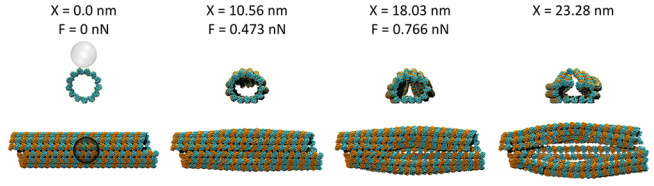

Figure 8. Steps along the major pathway for indentation on the seam for the MT 12D lattice with the plus end free. The figure follows the setup from Figure 5.

but also away from it on the positions used in our previous work:[13] between the PFs P6 and P7 and on each of these PFs separately, as described in section II.1 from the Supporting Information.

Indentation on the Seam (position p3) for the MT 12D Lattice. We observed the rip of the seam, accompanied by the strong ovalization of the free plus end (third and fourth stages in Figure 8), which is indicative of the fact that the crack on the seam propagates to the free end of the filament. Some longitudinal breaks develop close to the frozen minus end, likely due to the reduced mobility of the rings at this end. The evolution of native and non-native contacts for this pathway is in Figure S8G and follows the typical behavior at the seam reviewed above. Representative states along this pathway are in Figure 8. Similar to the crack propagation seen for the indentation on the P6/P7 interface discussed in section II.1 from the Supporting Information and represented in Figure S9D, the full propagation of the rip at the seam to the free plus end of the lattice is clear by the final stage. Moreover, here a larger gap opens in the upper surface of the lattice compared to the one in the final stage from Figure S9D, resulting in substantial outward bending of the sides of the filament.

DOI: 10.1021/acs.jpcb.9b03059
J. Phys. Chem. B 2019, 123, 4888−4900

The common theme among all our indentation pathways, as well as those from our previous work (Figure S8H),[13] is that the lateral interfaces located closest to or right under the indentation tip experience an increase in the total number of contacts in the early stages of the trajectory. At the same time, lateral interfaces located to the sides of the filament (away from the tip) buckle outward and reorganize their total contacts (loss of native contacts, but gain of non-native through formation of lateral contacts between the rotated PFs) in order to preserve the volume of the filament. Thus, the location of the first lateral break is only loosely dependent on the strength of the lateral interfaces in the starting configuration, but instead, it is determined dynamically by the redistribution of contacts between surfaces close and far from the indentation region. For example, for the simulations with the seam pointing down,[13] when pushing on the P6/P7 interface we found (Figure S8H) for a while an enhancement by ∼50% of the total number of contacts of the pushed P6/P7 interface, the neighboring P7/P8 interface, and of the other neighboring lateral P5/P6 interface, which is the weakest of all lateral interfaces. This enhancement is accompanied by a decrease in the native number of contacts of the P5/P6 interface (Figure S8H), allowing it to break first. For the simulations with the seam pointing up, when pushing on the PF P3, we found an initial enhancement by ∼100% of the seam (Figure 7). The additional stability gained at the seam prevents it from breaking in the early steps of the trajectory. We also found an increase in the number of non-native contacts at the P2/P3 and the P3/P4 lateral interfaces located under the tip (seen in the cyan and, respectively, the magenta curves from Figure 7).

Based on these findings, we infer that the binding of severing proteins to the seam cannot take advantage of any weakness in the seam if severing involves wedging/pushing because this action will lead to an increased stability of interfaces located near the binding region. Instead, binding of severing proteins away from the seam, when combined with a pushing action would take advantage of any weakness at the seam and would require lower breaking forces. Importantly, this result is likely independent of the length of the filament (well beyond our longest, 16D lattice), as we find the same behavior in MTs with one end (the plus end) free (see Figure S8, parts F and G).

Distributions of MT Kinking Angles during Indentation Closely Follow Experimental Distributions from Severing Assays. One goal for our study of the mechanical response of the seam region to radial compression is to shed light on the role played by the seam during the action of severing proteins. With this goal in mind, we set out to determine the degree of relatedness between our simulations and data from severing assays using the MT severing enzyme katanin p60. Following our previous work on MTs with lattice defects,[13] to compare our simulations with *in vitro* severing assays of the action of katanin on MT lattices, we used the kinking angle analysis, which accounts for the local distortions of the MT lattice. Our approach to extract the kinking angle from simulations is described in the Methods and section I.3 of the Supporting Information and it is illustrated in Figure S2 and Figure S3. From experiments we measured the kinking angles between two still intact fragments of MT that are thermally fluctuating under the action of katanin, as measured previously.[10,36] In experiments, the bending is driven by thermal fluctuations, and the kinking occurs in only a few PFs. This is similar to our simulations where only a couple of PFs are bent by the cantilever sphere (the PF on which we push in the case of the indentation positions p2 and p4, and the two PFs between which we push in the case of the indentation positions p1, p5 and p3).

From each type of simulation, we extracted the distribution of bending angles and we compared it with the experimental distributions. To establish the degree of statistical similarity between simulations and experiments, we employed the Kolmogorov−Smirnov (KS) test. This analysis allowed us to determine the simulation setup closest to severing experiments, which in turn enables us to provide molecular information regarding the severing of MTs such as pathways, the nature of intermediates, and force regimes (energetics). If the seam is a preferred functional site for severing enzymes, we expected to find that the bending angles obtained from our simulations of indentation directly on the seam (position p3) are the best match for the experimental angle distribution corresponding to the high-salt MTs (∼ 50% seam population). Moreover, because longer lattices (12D and 16D) are closer in length to the experimental MTs, we expected that the agreement with experiments improves with the length of the simulated MT. Our data (seen in the log−log plot of the KS values for 8D seam-up simulations with MT ends fixed versus each of the 2 experimental distributions from Figure S10A and Figure 9)

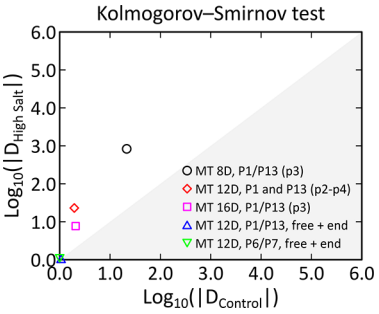

Figure 9. Best statistical matches between angle distributions from simulations and severing assays. The D values from the KS test analysis of bending angle distributions (CDFs) from various simulations set-ups versus those from the control (x-axis) and the high-salt (y-axis) MTs from severing assays plotted in log−log format. A very good statistical match will correspond to a small $\log(D)$ value (close to the origin of each axis). Here we selected from each MT length probed in simulations only the best match to the experimental data. All KS test results are given in Figure S10 from the Supporting Information.

shows that indeed for the 8D lattice the indentation on the seam leads to the best fit to the experimental data (value closest to the origin of the two axes). However, the KS values are relatively high and the actual distributions depicted in Figure 10A do not overlap perfectly. More importantly, the corresponding results for the 12D MTs simulations (Figure S10B and Figure 9) show that indentation on the seam is no longer the best fit for the experimental angles at this MT length. Thus, based on the behavior of the bending angles, we conclude that indentation on the seam far away from the ends of a filament is unlikely to reproduce the severing action of katanin on either high-salt or control MTs.

We found instead a striking correlation between the experimental angles and the simulated angles corresponding to the radial compression of MTs with the plus end free

DOI: 10.1021/acs.jpcb.9b03059
J. Phys. Chem. B 2019, 123, 4888−4900

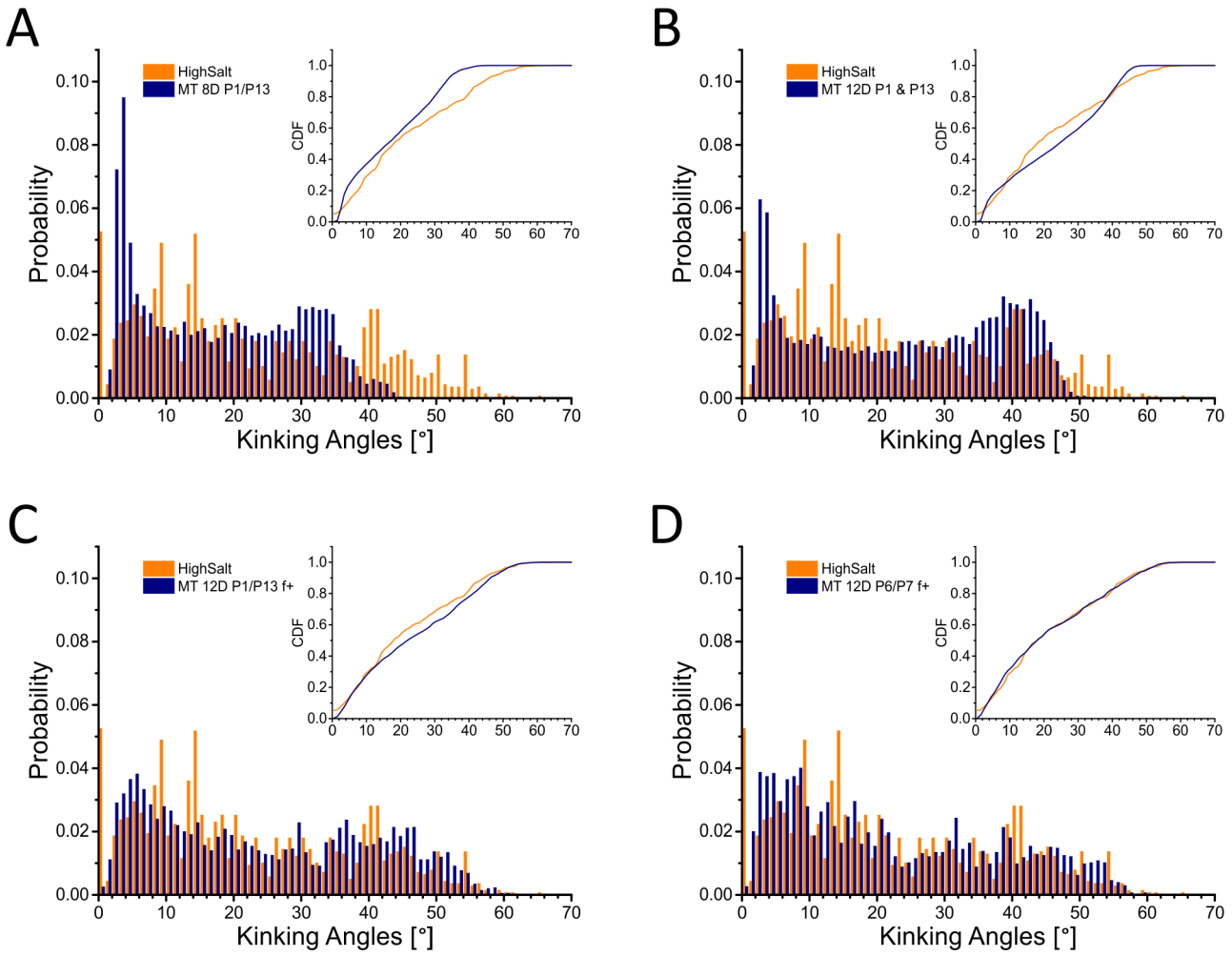

Figure 10. Distributions of bending angles from select simulation set-ups (dark blue) and from severing assays with high-salt MTs (orange). The inset for each plot represents the corresponding CDFs for the 2 histograms. (A) Results of pushing on the seam (position p3) of the MT 8D filaments with both ends fixed. (B) Results of pushing on PFs P1 or P13 for the MT 12D filaments with both ends fixed. (C) Results of pushing on the seam (position p3) of the MT 12D with the plus end free. (D) Results of pushing on the P6/P7 interface of MT 12D filaments with the plus end free. Histograms for all set-ups are in Figure S11 from the Supporting Information.

(Figure 9 and Figure S10, parts E and F, for the log−log plot of the KS values for the 8D and the 12D MTs, and Figure 10, parts C and D, and Figure S11, parts D and E, for the corresponding histograms). This result suggests that severing of high-salt or control MTs by katanin p60 could follow the pathways for radial compression of MTs with the plus end free. Thus, intermediate conformations during the severing of the lattice would correspond to the states such as those for late indentation stages from Figure 8. Importantly, these conformations and those in Figure 5 for pushing on the seam in the 8D lattice, which was the best match to experimental kinking angles for this MT length, are strikingly similar to the severing intermediates recently found in TEM-based experiments (for example seen in Figure 1D from[37]).

The best match between the experimental angle distributions and the angles from simulations with the ends of the filament fixed was for pushing on PFs near the seam (Figure 9 and Figure S10B for the log−log plot of the KS values for the 12D simulations versus the 2 experimental sets, and Figure 10B for the histograms). Interestingly, the best match is for angles measured between rings R3 and R10 in the 12D filament with ends fixed (numbering following Figure S1A), just as for the 16D filament with ends fixed the best fit to experiments is for rings R5 to R12 (Figure S10, parts B and C, for the KS values, and Figure S11, parts B and C, for the histograms). Thus, the best fit is always for a length of 8D irrespective of the actual length of the filament in our simulations. However, the degree of agreement between the computational and the experimental angle distributions increases with the length of the simulated MT filaments. For example, compare Figure S10A for 8D to Figure S10B for 12D MTs for the log−log plot of the KS values and Figure S11A for 8D with Figure S11B for 12D filaments for the actual histograms. This means that the bending regime of the central eight dimers in a filament depends strongly on the nature of the constraints at its ends: the distribution becomes broader and broader with the increase in the contour length of the filament. The behavior is also likely correlated with the degree of force propagation, i.e., the fact that, for a cylinder with the radius and the thickness of a 13_3 MT filament, the deformation induced by pushing in the middle of the lattice propagates over a distance comparable to the length of the 8D MT.[17] The likelihood that severing proteins acting directly on a PF located very close to one of the two weakest lateral interfaces (seam and P5/P6) take advantage of the flexibility of MT filaments (seen in the behavior of the angle distributions for the increasingly longer

DOI: 10.1021/acs.jpcb.9b03059
J. Phys. Chem. B 2019, 123, 4888−4900

lattices) is also supported by the fact that the worst match for indentation on filaments with ends fixed is for pushing on PF P3 (Figure S10A for the KS values and Figure S11.F for the histograms). This setup led to the smallest value of the critical breaking force, but only due to the very brittle behavior of the lattice compared to the high plasticity seen during the indentation on positions p2 or p4. The lack of agreement in the bending pattern when compressing P3 suggests that despite the possible favorable energetic costs severing enzymes do not target this type of brittle MT filaments.

Thermodynamics/Energetics of the Seam. We ran retraction simulations for 20 of our 12D MT indentation simulations, starting from conformations either beyond the first or beyond the critical breaking points for a total of 40 retraction trajectories. This is similar to the approach used in AFM experiments[26] and in our previous investigations into the mechanics of MTs.[13,16] Examples of indentation/retraction curves for each of the five indentation positions near the seam are in Figure S12, with details about the degree of recovery provided in Table S3 and discussion in section II.2 of the Supporting Information. To determine the Gibbs free energy change at the seam interface, we employed our previous approach based on Crooks's fluctuation dissipation theorem.[16,19] We recorded the total number of lateral contacts broken up to the point from which we start the retraction run and the force. We integrated the force versus indentation depth up to the point where only lateral contacts were broken (W, E contacts) to obtain the work for indentation. We counted only one set, either the east or the west contacts and not both because, up to this point, the broken lateral interfaces mirror each other and would therefore lead to double counting. We also integrated the retraction force versus depth curve to extract the work for retraction. Following our previous work,[16] for each indentation point, we determined the reversible work as the average of the highest retraction work and the lowest indentation work. By dividing the resulting reversible work by the number of broken contacts and averaging over all the indentation points, we obtained an average Gibbs free energy per contact, $\Delta G = -5.00 \pm 0.67$ kcal/mol. We also computed the enthalpy from the change in the potential energy in the SOP model between the first step and the last step of the indentation, $\Delta H = -15.50 \pm 1.15$ kcal/mol. Thus, the $T\Delta S = -10.51$ kcal/mol ± 0.95 (see Table S4 in the Supporting Information for the thermodynamic data from each type of trajectory). These values are all close to the thermodynamic values for the regular B-lattice lateral interfaces extracted in our previous work.[16] It is important to note that these energy values contain substantial contributions from bending of MT subunits and interfaces, rather than just the binding/unbinding energetics. Estimates of the percent of the ΔG value due primarily from binding/unbinding (reported in Table S4) are ~17%. Thus, care needs to taken when comparing the energies resulting from the bending and breaking of interfaces from the middle of MT filaments versus experimental measurements such as the very recent single-molecule measurements of the tubulin association and dissociation rates from growing MT ends, which reported the strength for a lateral bond of 3.6 ± 0.4 k_BT.[38]

MT Lattice Elongation. The analysis of our simulations with the plus end free showed that the MT lattice relaxes initially by increasing the distance between the subunits in each PF. To examine in detail this phenomenon, we carried out additional runs for 8D (1 trajectory), 12D (2 trajectories), and 16D (2 trajectories) MT filaments with the plus end free. For each frame of a trajectory we measured the displacement of the plus end of the filament from its initial position, and we divided by the number of rings in the polymer. Next, we averaged the data obtained for each PF and report it for each frame of the trajectory as an average elongation per 1 dimer. Taking into account that the time interval between frames was 0.040 ms, we obtained the kinetics for the elongation/dimer vs time by fitting our kinetic data to $y = a(1 - e^{-bx})$ (Figure S13A), as described in detail in section I.4 of the Supporting Information. Knowing that each dimer is 85 Å long, we converted the number of dimers in the polymer to its length. Moreover, since the b parameter is a rate constant, we calculated the elongation half time $\tau_{1/2}$ for each polymer. Next, we estimated the time when all our models will be fully relaxed (for 13 x $\tau_{1/2}$, the elongation is 99.99%). We found that the average elongation time for a 1 μm long MT filament is 38.25–40.96 ms (Figure S13B). Thus, for the typical *in vitro* and cellular length of MTs of 10–50 μm, our results predict that the elongation time would be 0.4–2 s. As in severing assays, the nanoscale damage of MTs with katanin or spastin starts around 20–30 s,[27,37] our results predict that MTs without constraints at the plus end will likely undergo elongation to a GTP-like state for the tubulin subunits prior to the start of severing.

Scaling of the Bending Force with the Length of the MT Filament. The drop in the value of the first breaking force with the increase in the length of the filament from our simulations mirrors qualitatively the behavior seen during bending of MTs in laser optical tweezers (LOT) experiments.[33] Such bending of MTs is relevant for example for the formation of long-lived rings and arcs observed in MT gliding assays or *in vivo* for the static curvatures of the quiescent eukaryotic flagella.[39] However, there is a marked difference between the magnitude of forces, which might be due to the substantial mismatch between the length of the MTs used in experiments (~10 μm) and the maximal length accessible in our molecular-level simulations (~200 nm). To bridge the gap between these two length-scales, which would allow us to make predictions regarding the mechanical behavior of longer MTs observed in cells, we resort to macroscopic models. The simplest macroscopic model for a MT lattice is a thin isotropic cylindrical shell.[40,41] To determine if such a model can be used, as a first approximation, to predict the first breaking force for long MTs (*in vitro* or cellular lengths of 10–50 μm), we tested if the results in prior work[41] can reproduce the values of the first breaking forces found in our simulations. For our 13_3 MT lattice, $t/R = 1.1$ nm/12.5 nm ~ 0.1.[17] For the 8D MT, $L/R = 68/12.5 \sim 6$. These values correspond to the red line in Figure 2C in[41] depicting the indentation of a thin semi-cylindrical shell with free ends. Here the first transition occurs at a dimensionless indentation depth $Z' = Z/R = 0.6$ and a dimensionless force of $F/Et^2 = 0.17$. Because $R = 12.5$ nm, it follows that $Z = 7.5$ nm, which is the indentation depth corresponding to the first break in our 8D lattices (see Figure 1). Using $E = 0.6$ GPa[33] and $t = 1.1$ nm in the dimensionless force equation, we obtain F = 123 pN. Because in our simulations the 8D lattice is fixed at both ends and the force for bending Euler beams fixed at both ends is 4 times larger than the one for bending beams with the ends hinged,[42] the calculated breaking force is 480 pN. This matches the average first breaking force resulting from our simulations of MT 8D (Table 1).

DOI: 10.1021/acs.jpcb.9b03059
J. Phys. Chem. B 2019, 123, 4888–4900

The indentation depth corresponding to the first breaking force remains relatively stable for all lengths (8D, 12D, and 16D), suggesting that the first breaking force for *in vitro* MTs is going to be ∼120 pN, which corresponds to a shell with free ends. This is also comparable to the value that one would get from the typical indentation force obtained in AFM experiments of 300 pN[26] adjusted to the level of the LOT experiments (which are closer to cellular conditions) based on the ∼2 orders of magnitude lower speed of the LOT experiments[33] when using the Bell−Evans model.[43] Still, this force is considerably higher than the values from the LOT experiments.[33] The discrepancy between the two force values could be due to differences between the process of bending in the LOT experiments and the cutting in our simulations, as discussed below.

Still, another source of the discrepancy in force values can be the fact that the MT filament is known to exhibit high elastic anisotropy, being characterized by a very large longitudinal Young's modulus (of order GPa) but low shear and circumferential elastic moduli (of order MPa).[33,44,45] This would require that the MT is modeled as an elastic orthotropic shell instead of an isotropic one.[45−47] Indeed, the study of MTs undergoing buckling upon bending using both the orthotropic and the isotropic thin shell models for MTs showed that the isotropic model overestimates the critical bending moment by close to 2 orders of magnitude compared to the orthotropic one.[46] Moreover, this is similar to the case of radial compression, where the critical buckling load from the isotropic model is 2 orders of magnitude higher than that given by the orthotropic model, with only the latter giving results compatible with experimental observations.[40,46] This relationship, together with our results and the above analysis, yields that the first breaking force during radial compression that would result in the lateral breaking of a long (at least 10 μm) MT would likely be 2 orders of magnitude smaller than the ∼100 pN from above, or ∼1 pN. Incidentally, this value coincides with the force measured in LOT experiments studying bending of such long MTs.[33]

The modeling of MTs buckling behavior using a molecular structural mechanics model (MSM)[42,48] showed that the critical buckling force obtained from MT lattices shorter than ∼0.2 to 1 μm suffers from finite-size effects, which agrees with our findings from simulations for the various MT lattice lengths. Finally, these studies conducted on lattices with different number of PFs, N (12, 13, 14), showed that E is independent of N,[42] which is exactly the result from the experimental study of high-salt versus control MTs.[14] This gives support to the comparison of our simulation results with the above-mentioned results from the macroscopic (MSM) modeling. However, it is important to note that all the macroscopic models used to model MTs (isotropic, orthotropic thin shells, MSM, and beads and springs) assume that no contact breaks at any of the interfaces between subunits in an MT lattice under radial compression, which is not the case in our simulations here and in previous works.[13,16]

As discussed above, another possible scenario that would account for the substantial difference between the force required to bend a MT under radial compression, as mimicked in our simulations, and under end bending (as carried out in LOT experiments) is that there are underlying differences between these two processes. Support for this view comes from a number of studies in the literature.[33,40,45] Namely, in our simulations of indentation/cutting of MTs, we detected, as presented above, a dynamic increase in the lateral interfaces located in close proximity of the cantilever tip. This change is likely the microscopic manifestation of the hardening of the circumferential modulus of MTs under large compressive radial deformation, discussed in the literature.[33,45] The net result is that the circumferential modulus of the MT increases by 3 orders of magnitude, from the typical ∼5 MPa[40] to a value close to that of the axial modulus of ∼1 GPa.[45] Under such conditions, the force required to bend, buckle, and eventually break the MT filament through radial compression is on the order of hundreds of pN corresponding to a radial deflection of 4−8 nm, which is exactly what we measure in our simulations and what is found in AFM experiments.[26] In contrast, in the absence of the hardening of the circumferential modulus, i.e., for E_c = 5 MPa, a concentrated radial force of 1 pN can induce a radial deflection up to 4 nm.[33,45] This scenario corresponds to pushing or pulling by concentrated forces acting directly on the lateral interface between PFs in a MT lattice. However, because all severing proteins are comparable in size to the cantilever sphere from our simulations and the AFM experiments, our results indicate that severing will require large forces if it involves wedging/pushing because radial compression will lead to the hardening of lateral interfaces. Thus, it is likely that severing and bending of long MTs follow different pathways.

CONCLUSIONS

The seam of MTs has long been considered a special region of the filament starting from the fact that it is the only A-lattice configuration in the most highly populated type of MT *in vivo*, the 13_3 lattice. Due to its unique structure, the seam has been proposed as a likely region to start the MT depolymerization under thermal fluctuations or under the action of depolymerizing motors and as a lattice defect which would make it a target for severing proteins. The underlying idea is that the seam is intrinsically weaker energetically than the rest of the lattice, which makes it prone to early breaks under the effect of modest perturbations. However, there is substantial controversy surrounding each of these proposals.

Our simulation approach, which describes the MT lattice in atomistic detail, enables us to control the type of lattice (i.e., the nucleotide state and the contour length) as well as the location of the force pushing on the filament. We probed directly the thermodynamics of the seam, its mechanical response, as well as extracted bending parameters that can be compared directly with experiments. In all these tests, we showed that the seam is not weak either thermodynamically or mechanically.

We found that the seam interface was mechanically and thermodynamically similar to other PF−PF interfaces. Because MTs indented on or near the seam recover fast upon the removal of the applied force, any cracks that form in MTs before the final collapse are highly reversible and healable. Therefore, breaking of defect-free MTs would be just as energetically costly, whether the radial force is applied on the seam or away from it. This is in contrast with the behavior of MT lattices with defects from our previous work,[13] which break under smaller forces and are unlikely to recover upon the removal of the external perturbation. These results imply that the seam would not be a favorable severing target.

Severing-kinking angle distributions from simulations showed that there is no difference between seam-up intact MT indentations and seam-down intact MT indentations in

DOI: 10.1021/acs.jpcb.9b03059
J. Phys. Chem. B 2019, 123, 4888−4900

terms of pathways. This finding also supports the idea that the seam is the same as a regular PF−PF interface. The major states populated along the pathways for which the distribution of the bending angles is closest to the experimental distributions resemble the severing intermediates with nanoscale damage imaged very recently using negative-stain TEM.[37] Thus, our study predicts that severing is initiated by lateral breaking between PFs located under or in close vicinity to the severing protein(s), followed by large crack propagation (for over 50 nm) and eventual break of longitudinal contacts in these 2−3 PFs. The location of the lateral crack is dependent only on the location of the severing enzyme, again implying that the seam behaves similarly to other interfaces in the MT lattice in our simulations. This result supports the view that the seam is not a lattice defect.[2,14,49]

To take advantage of any weakness in lateral interfaces such as at the seam, we carried out pushing on the lattice oriented such that the two weakest lateral interfaces, the seam and the P5/P6 interface, are on the sides of the filament. This setup led to a very brittle response of the MT lattice: once a crack formed under the tip, the whole filament collapsed. However, because the resulting bending angle distribution had nothing in common with the experimental distributions, our results rule out any weakness of the seam as a contributing factor to severing.

Overall, our simulation data, combined with recent mechanical measurements,[14] imply that the MT seam is not a lattice defect and is not a mechanically weak location of the MT lattice. These results contradict numerous hypotheses that assumed a weakened state for the seam from structural studies alone. Future experimental works using flow-induced bending or AFM indentation of high-salt MTs could shed more light on the true mechanical nature of MT seams. Moreover, as various tubulin isoforms lead to different MT lattice arrangements with differential stability against depolymerization or passive disassembly in the presence of kinesins,[3] it would be interesting to test the role of the seam in the mechanics of such lattices as well. Another interesting avenue would be to test the effect of tau, PRC1, or XMAP215 proteins on the mechanics of MTs. These MT-associated proteins likely bind regions span several dimers allowing them to act as longitudinal or lateral buttresses on the MT filament. Indeed, prior work using AFM indentation on MTs in the presence of tau showed that although tau only makes a 1 nm thick layer, it increases the radial elasticity and protects MTs from rupture.[50] Future simulations of indentation could probe the possible mechanisms used by tau to stiffen MTs.

■ ASSOCIATED CONTENT

Supporting Information

The Supporting Information is available free of charge on the ACS Publications website at DOI: 10.1021/acs.jpcb.9b03059.

Supplemental methods, data analysis for the computational part; supplemental results, detailed description of the indentation pathways; Table S1, average breaking forces for the runs with ends fixed; Table S2, average breaking forces for the runs with plus end free; Table S3, retraction pathways; Table S4, results of the thermodynamic analysis; Figure S1, MT structures used in simulations and severing assays; Figure S2, scheme for measuring the PF bending angle in simulations with both ends fixed; Figure S3, scheme for measuring the PF bending angle in simulations with the plus end free; Figure S4, sample data analysis for an indentation position; Figure S5, force versus indentation depth for pushing near the seam with both ends fixed; Figure S6, force versus indentation depth for pushing near the seam with plus end free; Figure S7, distributions of first breaking forces by MT length and indentation position; Figure S8, evolution of native and non-native contacts; Figure S9, snapshots of representative states along the major indentation pathways for the MT 8D and 12D filaments; Figure S10, results of KS test for the comparison between distribution of bending angles in simulations and in severing assays; Figure S11, histograms of bending angles in simulations and in severing assays; Figure S12, examples of indentation−retraction runs for pushing near the seam; Figure S13, results of PF elongation analysis (PDF)

■ AUTHOR INFORMATION

Corresponding Author

*(R.I.D.) E-mail: dimari@ucmail.uc.edu. Telephone: +1 (513) 556-3961. Fax: +1 (513) 556-9239.

ORCID

Ruxandra I. Dima: 0000-0001-6105-7287

Notes

The authors declare no competing financial interest.

■ ACKNOWLEDGMENTS

This work has been supported by National Science Foundation (NSF) Grants MCB-1412183 and MCB-1817948 to R.I.D. and Grant MCB-1817926 to J.L.R.

■ REFERENCES

(1) Nogales, E.; Whittaker, M.; Milligan, R. A.; Downing, K. H. High-resolution model of the microtubule. *Cell* **1999**, *96*, 79−88.

(2) Sui, H.; Downing, K. H. Structural basis of interprotofilament interaction and lateral deformation of microtubules. *Structure* **2010**, *18*, 1022−1031.

(3) Ti, S.-C.; Alushin, G. M.; Kapoor, T. M. Human β-tubulin isotypes can regulate microtubule protofilament number and stability. *Dev. Cell* **2018**, *47*, 175−190.e5.

(4) Nogales, E.; Wang, H.-W. Structural intermediates in microtubule assembly and disassembly: How and why? *Curr. Opin. Cell Biol.* **2006**, *18*, 179−184.

(5) Gardner, M. K.; Hunt, A. J.; Goodson, H. V.; Odde, D. J. Microtubule assembly dynamics: New insights at the nanoscale. *Curr. Opin. Cell Biol.* **2008**, *20*, 64−70.

(6) Katsuki, M.; Drummond, D. R.; Cross, R. A. Ectopic A-lattice seams destabilize microtubules. *Nat. Commun.* **2014**, *5*, 3094.

(7) Cross, R. A. Microtubule lattice plasticity. *Curr. Opin. Cell Biol.* **2019**, *56*, 88−93.

(8) Manka, S. W.; Moores, C. A. Microtubule structure by cryo-EM: Snapshots of dynamic instability. *Essays Biochem.* **2018**, *62*, 737−751.

(9) Zhang, R.; LaFrance, B.; Nogales, E. Separating the effects of nucleotide and EB binding on microtubule structure. *Proc. Natl. Acad. Sci. U. S. A.* **2018**, *115*, E6191−E6200.

(10) Davis, L. J.; Odde, D. J.; Block, S. M.; Gross, S. P. The importance of lattice defects in katanin-mediated microtubule severing in vitro. *Biophys. J.* **2002**, *82*, 2916−2927.

(11) Diaz-Valencia, J.; Morelli, M.; Bailey, M.; Zhang, D.; Sharp, D.; Ross, J. L. Drosophila datanin-60 depolymerizes and severs at microtubule defects. *Biophys. J.* **2011**, *100*, 2440−2449.

(12) Bailey, M. E.; Jiang, N.; Dima, R. I.; Ross, J. L. Microtubule severing enzymes couple ATPase activity with tubulin GTPase spring loading. *Biopolymers* **2016**, *105*, 547−556.

DOI: 10.1021/acs.jpcb.9b03059
J. Phys. Chem. B 2019, 123, 4888−4900

(13) Jiang, N.; Bailey, M.; Burke, J.; Ross, J. L.; Dima, R. I. Modeling the effects of lattice defects on microtubule breaking and healing. *Cytoskeleton* **2017**, *74*, 3−17.
(14) Harris, B. J.; Ross, J. L.; Hawkins, T. L. Microtubule seams are not mechanically weak defects. *Phys. Rev. E: Stat. Phys., Plasmas, Fluids, Relat. Interdiscip. Top.* **2018**, *97*, 062408.
(15) Dias, D. P.; Milligan, R. A. Motor protein decoration of microtubules grown in high salt conditions reveals the presence of mixed lattices. *J. Mol. Biol.* **1999**, *287*, 287−292.
(16) Kononova, O.; Kholodov, Y.; Theisen, K. E.; Marx, K. A.; Dima, R. I.; Ataullakhanov, F. I.; Grishchuk, E. L.; Barsegov, V. Tubulin bond energies and microtubule biomechanics determined from nano-indentation in silico. *J. Am. Chem. Soc.* **2014**, *136*, 17036−17045.
(17) dePablo, P. J.; Schaap, I. A. T.; MacKintosh, F. C.; Schmidt, C. F. Deformation and collapse of microtubules on the nanometer scale. *Phys. Rev. Lett.* **2003**, *91*, 098101.
(18) Maillard, R.; Chistol, G.; Sen, M.; Righini, M.; Tan, J.; Kaiser, C. M.; Hodges, C.; Martin, A.; Bustamante, C. ClpX(P) generates mechanical force to unfold and translocate its protein substrates. *Cell* **2011**, *145*, 459−469.
(19) Crooks, G. E. Entropy production fluctuation theorem and the nonequilibrium work relation for free energy differences. *Phys. Rev. E: Stat. Phys., Plasmas, Fluids, Relat. Interdiscip. Top.* **1999**, *60*, 2721−2726.
(20) Humphrey, W.; Dalke, A.; Schulten, K. VMD: Visual molecular dynamics. *J. Mol. Graphics* **1996**, *14*, 33−38.
(21) Hyeon, C.; Dima, R. I.; Thirumalai, D. Pathways and kinetic barriers in mechanical unfolding and refolding of RNA and proteins. *Structure* **2006**, *14*, 1633−1645.
(22) Zhmurov, A.; Dima, R. I.; Kholodov, Y.; Barsegov, V. SOP-GPU: Accelerating biomolecular simulations in the centisecond timescale using graphics processors. *Proteins: Struct., Funct., Genet.* **2010**, *78*, 2984−2999.
(23) Wells, D. B.; Aksimentiev, A. Mechanical properties of a complete microtubule revealed through molecular dynamics simulation. *Biophys. J.* **2010**, *99*, 629−637.
(24) Ayoub, A. T.; Klobukowski, M.; Tuszynski, J. A. Detailed per-residue energetic analysis explains the driving force for microtubule disassembly. *PLoS Comput. Biol.* **2015**, *11*, e1004313.
(25) Roll-Mecak, A.; Vale, R. D. Structural basis of microtubulue severing by the hereditary spastic paraplegia protein spastin. *Nature* **2008**, *451*, 363−368.
(26) Schaap, I. A. T.; Carrasco, C.; dePablo, P. J.; MacKintosh, F. C.; Schmidt, C. F. Elastic response, buckling, and instability of microtubules under radial indentation. *Biophys. J.* **2006**, *91*, 1521−1531.
(27) Bailey, M. E.; Sackett, D. L.; Ross, J. L. Katanin severing and binding microtubules are inhibited by tubulin carboxy tails. *Biophys. J.* **2015**, *109*, 2546−2561.
(28) Dixit, R.; Ross, J. L. Studying plus-end tracking at single molecule resolution using TIRF microscopy. *Methods Cell Biol.* **2010**, *95*, 543−554.
(29) Zhang, D.; Grode, K. D.; Stewman, S. F.; Diaz-Valencia, J. D.; Liebling, E.; Rath, U.; Riera, T.; Currie, J. D.; Buster, D. W.; Asenjo, A. B.; et al. Drosophila katanin is a microtubule depolymerase that regulates cortical-microtubule plus-end interactions and cell migration. *Nat. Cell Biol.* **2011**, *13*, 361−369.
(30) Loughlin, R.; Wilbur, J. D.; McNally, F. J.; Nedelec, F. J.; Heald, R. Katanin contributes to interspecies spindle length scaling in Xenopus. *Cell* **2011**, *147*, 1397−407.
(31) Diaz-Valencia, J.; Bailey, M.; Ross, J. Purification and biophysical analysis of microtubule-severing enzymes in vitro. *Methods Cell Biol.* **2013**, *115*, 191−213.
(32) Ross, J. L.; Dixit, R. Multiple color single molecule TIRF imaging and tracking of MAPs and motors. *Methods Cell Biol.* **2010**, *95*, 521−542.
(33) Memet, E.; Hilitski, F.; Morris, M. A.; Schwenger, W. J.; Dogic, Z.; Mahadevan, L. Microtubules soften due to cross-sectional flattening. *eLife* **2018**, *7*, e34695.
(34) Huang, Y.-S.; Hsu, F.-L.; Lee, C.-M.; Juang, J.-Y. Failure mechanism of hollow tree trunks due to cross-sectional flattening. *R. Soc. Open Sci.* **2017**, *4*, 160972.
(35) Alushin, G. M.; Lander, G. C.; Kellogg, E. H.; Zhang, R.; Baker, D.; Nogales, E. High-resolution microtubule structures reveal the structural transitions in $\alpha\beta$-Tubulin upon GTP hydrolysis. *Cell* **2014**, *157*, 1117−1129.
(36) Mohrbach, H.; Kulic, I. M. Motor driven microtubule shape fluctuations: force from within the lattice. *Phys. Rev. Lett.* **2007**, *99*, 218102.
(37) Vemu, A.; Szczesna, E.; Zehr, E. A.; Spector, J. O.; Grigorieff, N.; Deaconescu, A. M.; Roll-Mecak, A. Severing enzymes amplify microtubule arrays through lattice GTP-tubulin incorporation. *Science* **2018**, *361*, eaau1504.
(38) Mickolajczyk, K. J.; Geyer, E. A.; Kim, T.; Rice, L. M.; Hancock, W. O. Direct observation of individual tubulin dimers binding to growing microtubules. *Proc. Natl. Acad. Sci. U. S. A.* **2019**, *116*, 7314−7322.
(39) Sartori, P.; Geyer, V. F.; Scholich, A.; Julicher, F.; Howard, J. Dynamic curvature regulation accounts for the symmetric and asymmetric beats of *Chlamydomonas flagella*. *eLife* **2016**, *5*, e13258.
(40) Needleman, D. J.; Ojeda-Lopez, M. A.; Raviv, U.; Ewert, K.; Miller, H. P.; Wilson, L.; Safinya, C. R. Radial compression of microtubules and the mechanism of action of taxol and associated proteins. *Biophys. J.* **2005**, *89*, 3410−3423.
(41) Vaziri, A.; Mahadevan, L. Localized and extended deformations of elastic shells. *Proc. Natl. Acad. Sci. U. S. A.* **2008**, *105*, 7913−7918.
(42) Zhang, J.; Meguid, S. A. Buckling of microtubules: An insight by molecular and continuum mechanics. *Appl. Phys. Lett.* **2014**, *105*, 173704.
(43) Bell, G. Models for the specific adhesion of cells to cells. *Science* **1978**, *200*, 618−627.
(44) Pampaloni, F.; Lattanzi, G.; Jonas, A.; Surrey, T.; Frey, E.; Florin, E. L. Thermal fluctuations of grafted microtubules provide evidence of a length-dependent persistance length. *Proc. Natl. Acad. Sci. U. S. A.* **2006**, *103*, 10248−10253.
(45) Huang, G. Y.; Mai, Y.-W.; Ru, C. Q. Surface deflection of a microtubule loaded by a concentrated radial force. *Nanotechnology* **2008**, *19*, 125101.
(46) Wang, C. Y.; Ru, C. Q.; Mioduchowski, A. Orthotropic elastic shell model for buckling of microtubules. *Phys. Rev. E* **2006**, *74*, 052901.
(47) Yi, L.; Chang, T.; Ru, C. Q. Buckling of microtubules under bending and torsion. *J. Appl. Phys.* **2008**, *103*, 103516.
(48) Zhang, J.; Wang, C. Molecular structural mechanics model for the mechanical properties of microtubules. *Biomech. Model. Mechanobiol.* **2014**, *13*, 1175−1184.
(49) Manka, S. W.; Moores, C. A. The role of tubulin-tubulin lattice contacts in the mechanism of microtubule dynamic instability. *Nat. Struct. Mol. Biol.* **2018**, *25*, 607−615.
(50) Schaap, I.; Hoffmann, B.; Carrasco, C.; Merkel, R.; Schmidt, C. F. Tau protein binding forms a 1 nm thick layer along protofilaments without affecting the radial elasticity of microtubules. *J. Struct. Biol.* **2007**, *158*, 282−292.

DOI: 10.1021/acs.jpcb.9b03059
J. Phys. Chem. B 2019, 123, 4888−4900